

Thermocapillary migration and interaction dynamics of droplets in a constricted domain

Cite as: Phys. Fluids **31**, 022106 (2019); <https://doi.org/10.1063/1.5084313>

Submitted: 06 December 2018 . Accepted: 10 February 2019 . Published Online: 28 February 2019

Srinivasa Sagar Kalichetty, T. Sundararajan, and Arvind Pattamatta



View Online



Export Citation



CrossMark

ARTICLES YOU MAY BE INTERESTED IN

[Numerical study of droplet dynamics in a steady electric field using a hybrid lattice Boltzmann and finite volume method](#)

Physics of Fluids **31**, 022105 (2019); <https://doi.org/10.1063/1.5080210>

[Droplet generation at Hele-Shaw microfluidic T-junction](#)

Physics of Fluids **31**, 022010 (2019); <https://doi.org/10.1063/1.5086808>

[Surfactant-induced migration of a spherical droplet in non-isothermal Stokes flow](#)

Physics of Fluids **31**, 012110 (2019); <https://doi.org/10.1063/1.5064694>



Thermocapillary migration and interaction dynamics of droplets in a constricted domain

Cite as: Phys. Fluids 31, 022106 (2019); doi: 10.1063/1.5084313

Submitted: 6 December 2018 • Accepted: 10 February 2019 •

Published Online: 28 February 2019



View Online



Export Citation



CrossMark

Srinivasa Sagar Kalichetty,^{a)} T. Sundararajan,^{b)} and Arvind Pattamatta^{c)}

AFFILIATIONS

Department of Mechanical Engineering, IIT Madras, Chennai 600036, India

^{a)}Electronic mail: ksrinivasasagar@gmail.com

^{b)}Electronic mail: tsundar@iitm.ac.in

^{c)}Electronic mail: arvindp@iitm.ac.in

ABSTRACT

Migration of confined droplets in a stationary fluid medium due to thermocapillary forces is considered. An in-house solver with isosurface based interface reconstruction developed in OpenFOAM has been employed to carry out numerical simulations. Thermocapillary migration of a single droplet in a constricted domain with constriction comparable to the droplet size shows that the migration velocity has non-monotonic dependence on the droplet radius. In the case of two droplets migrating in a constricted domain, the relative slowdown of a larger droplet when a smaller droplet is trailing behind reveals the possibility of interaction which is not observed in larger domains. The effects of the constricted domain size, the initial distance of separation, the radius of the trailing droplet, and the Marangoni number are analysed for this configuration. It is observed that the constriction size and Marangoni number have more influence on the interaction and dictate whether the droplets may coalesce or move with a constant separation distance. The final steady state separation distance between the droplets does not depend on the initial separation distance, but it varies with the radius of the trailing droplet. The results from the present study reveal the physical mechanisms influencing the thermocapillary migration of droplets in constricted domains and interactions between the migrating droplets.

Published under license by AIP Publishing. <https://doi.org/10.1063/1.5084313>

I. INTRODUCTION

Motion of fluid particles such as bubbles or drops suspended in another fluid is encountered in a variety of engineering applications such as material processing,¹ mixing,² microfluidics,^{3,4} and heat transfer.⁵ Generally, in the presence of gravity, buoyancy is the dominant driving force for the motion of such suspended fluid particles. In microgravity, however, the buoyancy force is ineffective. Although it is possible to propel droplets with the help of surfactants,^{6,7} and magnetic or electric fields, a relatively simpler mechanism to generate motion is through the application of temperature gradients in the continuous phase. The motion of the fluid particle in such systems is caused due to the Marangoni effect, where interfacial motion is generated from lower to higher surface tension regions. Surface tension being a negative function of temperature, interfacial flows occurs opposite to the direction of the temperature gradient. Interfacial flow

can also cause the motion of the ambient fluid due to viscous traction, and the resulting reaction propels the fluid particle towards the hotter side.⁸ This phenomenon is referred to as thermocapillary migration and was first experimentally demonstrated by Young *et al.*⁹ by obstructing the rise of a bubble in a liquid column due to buoyancy through the application of a temperature gradient. Under normal gravity, the buoyancy effect overshadows the thermocapillary effect making the phenomenon difficult to observe. To minimize buoyancy effects, experiments were performed in free fall environments such as orbital space crafts,¹⁰ drop towers,¹¹ and sounding rockets¹² with an aim to understand the fundamentals of thermocapillary phenomena and to develop methods for material processing in space.¹²

Analytical models have been developed alongside the experiments to analyse bubble/droplet migration under microgravity. Young *et al.*⁹ proposed the YGB model to predict

the steady-state droplet velocity using linear analysis in the limit of vanishing Reynolds and Marangoni numbers. This analysis was extended using perturbation techniques to include the inertial and convective effects at non-zero Reynolds and Marangoni number values.¹³ Efforts were also made to develop solutions which address the complete parameter space of non-dimensional numbers,¹⁴ and the results are summarized in a review.¹⁵ Numerical methods provide useful insights into the complex nature of the physical mechanisms involved in fluid particle migration due to the thermocapillary phenomenon. One of the earliest numerical studies of bubble migration for non-zero Reynolds and Marangoni numbers was performed by Szymczyk and Siekmann.¹⁶ Different approaches such as Front Tracking,¹⁷ Volume of Fluid (VOF),^{18,19} Level Set,²⁰ and Lattice Boltzmann^{21,22} methods were adopted to model various aspects of thermocapillary migration. For instance, studies by Zhao *et al.*²⁰ showed the topological evolution of temperature field in a migrating droplet and its effect on migration dynamics. Studies by Haj-Hariri *et al.*²³ and Samareh *et al.*²⁴ explored the impact of deformability of fluid particle interface on migration. Recent work by Tripathi and Sahu²⁵ studied the motion of air bubbles under the combination of thermocapillary and buoyancy forces and the work by Balla *et al.*²⁶ extended it to the case of self-wetting fluids. The droplet migration dynamics is observed to be affected by fluid properties and initial and boundary conditions. The most common finding is that for finite Reynolds and Marangoni number values, the introduction of convective and inertial effects modifies the evolution of temperature and velocity fields significantly.¹⁷

Other than properties and non-dimensional number regimes, the fluid particle migration behaviour is affected when hydrodynamic and/or thermal interactions are present. The presence of a solid wall or domain boundary induces hydrodynamic retardation on the migrating fluid particle. The no-slip condition at the wall induces hydrodynamic drag on the ambient fluid, which reduces the reaction force propelling the fluid particle, thereby resulting in particle slowdown. Chen *et al.*²⁷ studied the migration of a bubble analytically in an insulated tube assuming axisymmetry and observed monotonic decrease in the non-dimensionalized migration velocity with an increase in the droplet radius for a fixed tube size. Following this, Keh *et al.* studied the velocity variation when a spherical droplet migrates parallel²⁸ and perpendicular²⁹ to two planar walls and observed that droplet velocity is impacted by the conductivity and viscosity ratios as well as the proximity to the walls. Mahesri *et al.*³⁰ used the boundary integral technique and extended the analysis to a deformable droplet. Recently, Capobianchi *et al.*³¹ studied droplet migration in converging and diverging wall configurations using the coupled level set method. It was observed that the droplet migrates faster due to thermal interactions in converging domains than in diverging ones, even though the hydrodynamic retardation increases. Alhendal *et al.*³² and Brady *et al.*³³ also numerically studied confinement effects on droplet migration and observed similar hydrodynamic retardation.

The presence of another migrating fluid particle in the same domain impacts the migration dynamics due to

hydrodynamic and thermal interactions between the particles. Experimental studies involving droplet interactions have seldom been reported. One such study was performed by Kang *et al.*³⁴ on the interaction of arbitrarily arranged air bubbles in silicone oil. One of the earliest analytical studies dealing with such interaction was performed by Meyyappan *et al.*⁸ for two bubbles aligned with the temperature gradient, using a heuristic composite approximation. It was observed that the smaller bubble always moves faster than the isolated bubble, irrespective of its trailing and leading position. The larger droplet, on the other hand, moves slower than its isolated case. Many quasi-analytical studies have been reported later on the interaction of bubbles and droplets in aligned and arbitrary arrangements.^{35,36} Numerical studies of arbitrarily aligned droplets were performed by Nas and Tryggvason³⁷ with the help of a Front tracking method where it was observed that the droplets lineup at steady state and space evenly across the channel perpendicular to the temperature gradient. Alhendal *et al.*³⁸ studied interaction using the volume of fluid method in ANSYS Fluent and observed that droplets would not interact when the smaller droplet follows the larger one since the larger droplet travels with larger velocity. Numerical simulations by Yin and Chamg³⁹ using the front tracking method showed that same sized interacting droplets in aligned configuration travel with a constant separation distance. Studies by Yin and Li⁴⁰ showed that droplets move with a constant separation distance when the larger droplet follows the smaller one, due to the interaction of the trailing droplet with the thermal wake of the leading droplet. An extensive parametric study has been performed to analyse the influence of particle interaction. It was observed that the dependence of thermal wake on the Marangoni number makes it the most influential parameter in determining the separation distance.

The effects of the presence of a wall or another fluid particle have been extensively studied. To the author's knowledge, there are no prior studies which consider both effects together. In constricted domains, the larger droplet may not always migrate faster than the smaller one, as there is a more significant wall drag on the larger droplet.²⁷ Earlier studies concluded that the interaction occurs only when the larger droplet follows the smaller one. Such a conclusion may not be valid in the cases where the larger droplet travels slower than the smaller one. The effect of constriction alters not only the velocity but also the convective effects on energy and momentum transfer and hence the interaction dynamics. In the present work, an OpenFOAM based in-house solver is used to study the thermocapillary interaction of two droplets in a constricted domain, migrating in an aligned configuration. The solver is validated with available experimental and numerical benchmarks. Subsequently, numerical studies are performed to evaluate the effect of constriction on migration dynamics. The interaction of two unequal sized droplets travelling in an aligned configuration is studied for exploring the effects of constriction, droplet leading and trailing configurations, trailing droplet radius, initial separation distance, and temperature gradient on interaction dynamics.

II. GOVERNING EQUATIONS AND NUMERICAL METHODOLOGY

A spherical droplet surrounded by another immiscible fluid with a uniform temperature gradient in zero gravity condition is considered. The droplet and continuous fluids are assumed to be Newtonian. The fluid properties are taken to be temperature independent, except for surface tension which is considered to vary linearly with temperature. The momentum and energy equations in the two fluids are solved through a single fluid approach, by employing the Volume of Fluid (VOF) method,⁴¹ with properties changing across the interface. The relevant formulations for mass, momentum, and energy are as follows:

Conservation of Mass:

$$\nabla \cdot \rho \vec{u} = 0, \quad (1)$$

Conservation of Momentum:

$$\frac{\partial(\rho \vec{u})}{\partial t} + \nabla(\vec{u} \cdot \rho \vec{u}) = -\nabla p + \nabla \cdot \left[\mu \left(\nabla \vec{u} + (\nabla \vec{u})^T \right) \right] + \vec{f}_\sigma, \quad (2)$$

Conservation of Energy:

$$\frac{\partial(\rho C T)}{\partial t} + \nabla \cdot (\rho C \vec{u} T) = \nabla(k \nabla T), \quad (3)$$

where \vec{u} is the velocity vector, p is the pressure, and T is the temperature. Also, ρ is the fluid density, μ is the dynamic viscosity, C is the specific heat, and k is the thermal conductivity. The properties corresponding to the droplet fluid are denoted with subscript d , and the ambient/continuous fluid properties are subscripted with c . The VOF approach uses an indicator variable α to distinguish between the two fluids. This variable α is the volume fraction which is 0 for one fluid and 1 for the other and varies between 0 and 1 across the interface. To track the evolution of the interface, an additional conservation equation for the volume fraction is solved, which is of the form

$$\frac{\partial \alpha}{\partial t} + \nabla \cdot (\vec{u} \alpha) + \nabla \cdot (\vec{u}_r \alpha (1 - \alpha)) = 0. \quad (4)$$

The third term of Eq. (4) is a special compression term added to ensure boundedness of the volume fraction and to maintain a sharp interface.⁴¹ Here, \vec{u}_r is the compression velocity, and it scales with the flow velocities in the direction normal to the interface.⁴¹ The thermophysical properties used in Eqs. (1)–(3) are calculated using a weighted average of material properties of the two fluids given by

$$\lambda = \alpha \lambda_d + (1 - \alpha) \lambda_c, \quad (5)$$

where λ_d and λ_c correspond to the thermophysical properties of the droplet and continuous fluid, respectively. The effect of surface tension is incorporated as a source term \vec{f}_σ in the momentum equation [Eq. (2)] which is modelled according to the continuum surface force (CSF) methodology proposed by Brackbill *et al.*⁴² as

$$\vec{f}_\sigma = \left[\sigma \kappa \vec{n} + (1 - \vec{n} \otimes \vec{n}) \nabla \sigma \right] |\nabla \alpha|, \quad (6)$$

where σ is the surface tension, κ is the curvature, and \vec{n} is the normal to the interface. The expression $|\nabla \alpha|$ ensures that the

source term is applied only at the interface. The first term of Eq. (6) corresponds to the normal component, which handles the pressure jump condition across the interface, while the second term corresponds to the tangential component which accounts for the shear force generated due to the variation of surface tension along the interface. Surface tension is considered to decrease linearly with temperature and is of the form

$$\sigma = \sigma_0 + \sigma_T (T - T_0), \quad (7)$$

where T_0 is the reference temperature (equal to lowest imposed boundary temperatures), σ_0 is the value of surface tension corresponding to T_0 , and σ_T is the temperature coefficient of the surface tension ($\frac{\partial \sigma}{\partial T}$). For the present case, the two phase solver implemented in OpenFOAM-2.2.0 is employed along with a contour based method for the calculation of curvature and normal at the interface developed by Kunkelmann *et al.*⁴³ This method is similar to PLIC (Piecewise Linear Interface Calculation) except that it reconstructs the interface from the single value of volume fraction ($\alpha = 0.5$) instead of matching interface location to volume fraction. This method has the advantage of accurate calculation of the curvature (κ) and the normal (\vec{n}) resulting in less spurious currents and better tracking of the interface.⁴¹ The mass and momentum equations are coupled and solved using the PIMPLE algorithm which is a combination of the PISO (Pressure Implicit with Splitting of Operators) and the SIMPLE (Semi Implicit Method for Pressure Linked Equations) algorithms. The volume fraction conservation equation is solved using the MULES (Multi-dimensional Limiter for Explicit Solution) algorithm, and the temporal discretization is done using the implicit Euler scheme. Adaptive time stepping is utilized in the present simulations with time step being varied based on a fixed Courant number of 0.1. To describe the problem in non-dimensional terms, property ratios are used, which are represented by the corresponding property symbols subscripted with r and described as follows:

$$\rho_r = \frac{\rho_d}{\rho_c}, \quad \mu_r = \frac{\mu_d}{\mu_c}, \quad C_r = \frac{C_d}{C_c}, \quad \text{and} \quad k_r = \frac{k_d}{k_c}. \quad (8)$$

All lengths are non-dimensionalized with the length a (maximum droplet radius) and velocities are non-dimensionalized with the reference velocity U_r which is defined as follows:

$$U_r = \frac{\sigma_T \Delta T_\infty a}{\mu_c}, \quad (9)$$

where ΔT_∞ is the temperature gradient in the continuous fluid. Based on the reference scales, the droplet migration velocity (U), length (x), time (t), and temperature (T) are non-dimensionalized as

$$U^* = \frac{U}{U_r}, \quad x^* = \frac{x}{a}, \quad t^* = \frac{t}{a/U_r}, \quad T^* = \frac{T - T_0}{\Delta T_\infty a}, \quad (10)$$

where $*$ indicates a dimensionless variable. For the present study, the relevant non-dimensional numbers governing the physics are the Reynolds number (Re), Marangoni number (Ma), and Capillary number (Ca) which are defined as follows:

$$Re = \frac{\rho_c a U_r}{\mu_c}, \quad Ma = \frac{\rho_c C_c a U_r}{k_c}, \quad Ca = \frac{\mu U_r}{\sigma_0}. \quad (11)$$

III. VALIDATION OF THE SOLVER

A. Validation with previous numerical studies

The present implementation of CSF formulation to simulate thermocapillary flows is tested by comparing with the 2-D numerical simulation of droplet thermocapillary rise by Nas and Tryggvason.³⁷ The computational domain is as shown in Fig. 1(a) with length and breadth dimensions of $8a$ and $4a$, respectively. The domain is initialized with a linear temperature gradient, and the droplet is initialized as a volume fraction field with $\alpha = 1$ at a distance of $2a$ from the bottom wall. Neumann conditions are applied on the lateral walls for both temperature and velocity. No slip condition for the velocity and the Dirichlet condition for the temperature are applied at the top and bottom walls with temperatures being maximum and minimum, respectively. For the volume fraction, Neumann boundary condition is applied on the walls. All the property ratios are considered to be 0.5 with non-dimensional parameters of $Re = 5$, $Ma = 20$, and $Ca = 0.01666$. The simulations were carried out on the domain discretized with a uniform Cartesian grid. The thermal gradient present in the ambient fluid moves the droplet towards the hotter side due to the thermocapillary action. The droplet migration velocity is calculated by the volume weighted averaging of the velocities of the cells as follows:

$$U = \frac{\sum_{i=1}^n \alpha \bar{v} V}{\sum_{i=1}^n \alpha V}, \quad (12)$$

where n corresponds to the total number of cells in the mesh and V corresponds to the volume of each cell. A grid independence study was performed for mesh resolutions of 12, 16, 20, and 24 cells per droplet radius (a). The velocity of the droplet at steady state has been tabulated in Table I. As the relative difference in the velocity (U^*) beyond a grid size of 16 cells/ a is found to be very small, the same has been considered to be

grid independent for this study. The evolution of the velocity obtained for the grid with 16 cells/ a is plotted in Fig. 1(b), and it can be observed that the results corroborate well with those of Nas and Tryggvason.³⁷

To validate the solver for a 3-D test case, the study by Liu et al.⁴⁴ is considered where simulations are performed in a parallelepiped domain of $7.5a \times 7.5a \times 15a$. The side walls are insulated, and the top and bottom wall temperatures are fixed at $T = 24$ and $T = 0$, respectively. The fluid properties are assigned as $\rho_r = \mu_r = k_r = C_r = 1$, $\sigma_0 = 2.5 \times 10^{-2}$, $\sigma_T = -1.5625 \times 10^{-3}$ with non-dimensional numbers of $Re = 1$, $Ma = 1, 10, 100$. To save the computational cost and taking the advantage of inherent axisymmetry in the problem, the studies were performed in an axisymmetric domain of $7.5a \times 15a$ as shown in Fig. 2. The domain is also intended to be used for studying the single droplet migration in a constricted domain. Hence for generalization, the domain is considered to be axisymmetric with radius a/CS and length l . The droplet of radius $a * \zeta$ is initialised at a distance of b from the bottom wall. ζ represents the size of the droplet, and CS represents the constriction size of the domain and both constants vary between 0 and 1. Here, a is considered as a reference dimension, representing the maximum droplet size considered. For the present case, the constants CS, l, b , and ζ are set to 0.267, $15a, 7.5a$, and 1, respectively. Grid independence study is performed for the case $Re = 1$ and $Ma = 100$ by comparing the velocity of the droplet at steady state as done for the previous validation, and it is found that the grid size of 30 cells per droplet radius (a) is grid independent. Simulations were performed for the cases of $Re = 1, Ma = 1, 10$, and 100 using the same grid and are plotted in Fig. 3(a) along with the predictions of Liu et al.⁴⁴ Each velocity in Fig. 3(a) is non-dimensionalized with corresponding velocities obtained from the YGB formula which predicts the velocity of thermocapillary rise at vanishing Marangoni and Reynolds numbers and is defined as follows:

$$U_{YGB} = \frac{2\sigma_T \Delta T_\infty \zeta a}{\mu_c (2 + \frac{k_d}{k_c}) (2 + 3 \frac{\mu_d}{\mu_c})}. \quad (13)$$

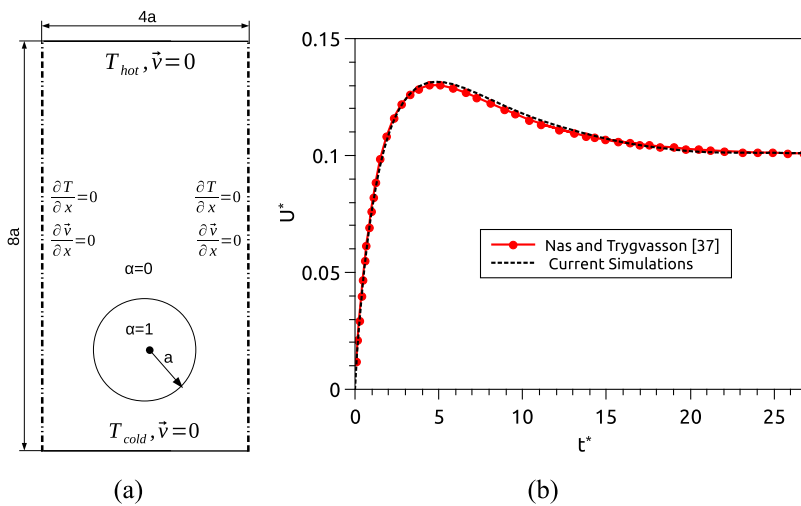


FIG. 1. (a) Schematic of the computational domain used for validation of the solver with the numerical simulations. (b) Temporal evolution of the velocity of a two dimensional droplet with $Re = 5$, $Ma = 20$, and $Ca = 0.01666$ compared with the results predicted by Nas and Tryggvason.³⁷

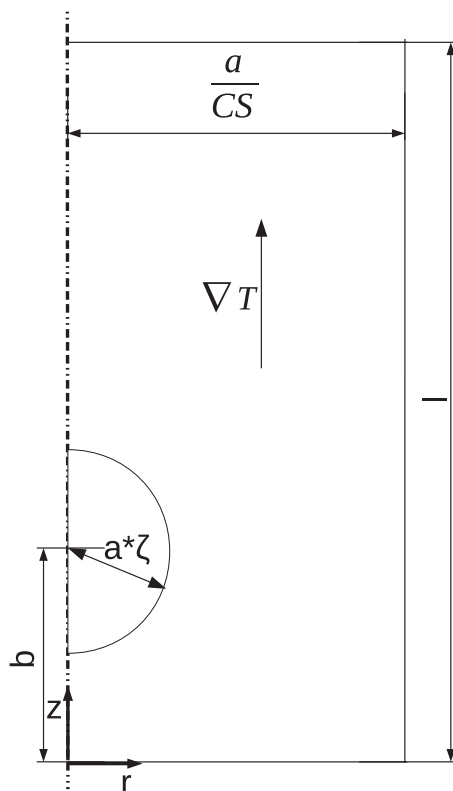
TABLE I. Grid independence test corresponding to the case of Nas and Tryggvason.³⁷

Grid size (Cells/ a)	Velocity (U^*)	Relative percentage difference (%)
12	0.097	...
16	0.1005	3.6
20	0.1008	0.3
24	0.101	0.2

It can be observed that the velocity evolution agree well with predictions of Liu *et al.*⁴⁴ for all the Marangoni numbers considered. The axial temperature distribution inside and vicinity of the droplet are plotted in Figs. 3(b)–3(d) for the cases of $Ma = 1, 10,$ and 100 along with the predictions from Liu *et al.*⁴⁴ The corresponding isotherms obtained at steady state are represented as an inset. From the plots, it can be observed that the axial temperature profiles obtained agree well with the predictions of Liu *et al.*⁴⁴

B. Validation with previous experimental studies

To assess the capability of the solver to simulate the experiments, the study by Hadland *et al.*¹⁰ is considered. The thermocapillary migration of an FC-75 droplet in a silicone oil matrix is studied in microgravity in a parallelepiped box with the bottom wall at a lower temperature and top wall at a higher

**FIG. 2.** Schematic of the computational domain.

temperature. The size of the box is 100 times the droplet size in the direction perpendicular to migration. It is computationally expensive and unnecessary to simulate the whole domain, as the analysis by Keh *et al.*²⁸ shows that for the domain sizes greater than five times the droplet radius, the droplet travels without side wall effects as in an unbounded domain. To save computational cost, instead of a full parallelepiped domain, an axisymmetric cylindrical domain of radius $5a$ was considered as shown in Fig. 2.

In the present test case, the values of ζ and CS are set to 1 and 0.2, respectively, which is in accordance with the criteria stated for the unbounded domain²⁸ assumption. The domain length of length $l = 16a$ is considered and the droplet is initialized at a distance of $b = 3a$ from the bottom wall. All the walls are considered to satisfy the no-slip condition. The side wall is insulated, and fixed temperatures are applied at the top and bottom walls. The values of fluid properties are taken from the experiments of Hadland *et al.*¹⁰ The corresponding property ratios are listed in Table II.

A grid independence study is performed for the case of $Ma = 100$ and simulations are performed using a uniform Cartesian grid with mesh sizes of 10, 20, 30, 40, 50 cells per droplet radius a . The steady state velocity obtained for each mesh density is tabulated in Table III. The steady state velocity is reduced by 0.3% when mesh resolution changes from $30/a$ to $40/a$, whereas it changes only by 0.1% with further refinement to $50/a$. Hence the mesh with $30/a$ cells is considered as grid independent, for the subsequent cases studied. Numerical simulations are performed for Marangoni numbers ranging from 2 to 500, keeping the capillary number $Ca = 0.2$. A large capillary number is chosen to avoid the generation of spurious currents at the interface.²⁰ Figure 4 shows the temporal velocity evolution of the droplet for various Marangoni numbers. To avoid non-physical values of migration velocity due to larger capillary number used, the evolution is tracked until the droplet centroid reaches $z^* = 6$.²⁰ Figure 5 shows the comparison of steady state velocities with the experimentally observed velocity predictions for different Marangoni numbers. The migration velocities at steady state for different Marangoni numbers, obtained in the present numerical simulations, are found to be close to the experimental observations of Hadland *et al.*¹⁰ for most values of Ma . The deviation from the numerical predictions previously reported in the literature^{20,31} can be attributed to the adoption of different interface tracking algorithms. The interfacial temperature is altered due to the convective effects at finite Marangoni numbers, which reduces the driving force for droplet motion. As a consequence, droplet moves at a lower velocity than U_{YGB} . The validation of the solver presented in this section shows its capability to predict the migration dynamics of a droplet due to the thermocapillary phenomenon.

IV. THERMOCAPILLARY MIGRATION OF SINGLE DROPLET IN A CONSTRICTED DOMAIN

The scenario described in Sec. III B considered large domains so that the wall effects on the droplet migration are

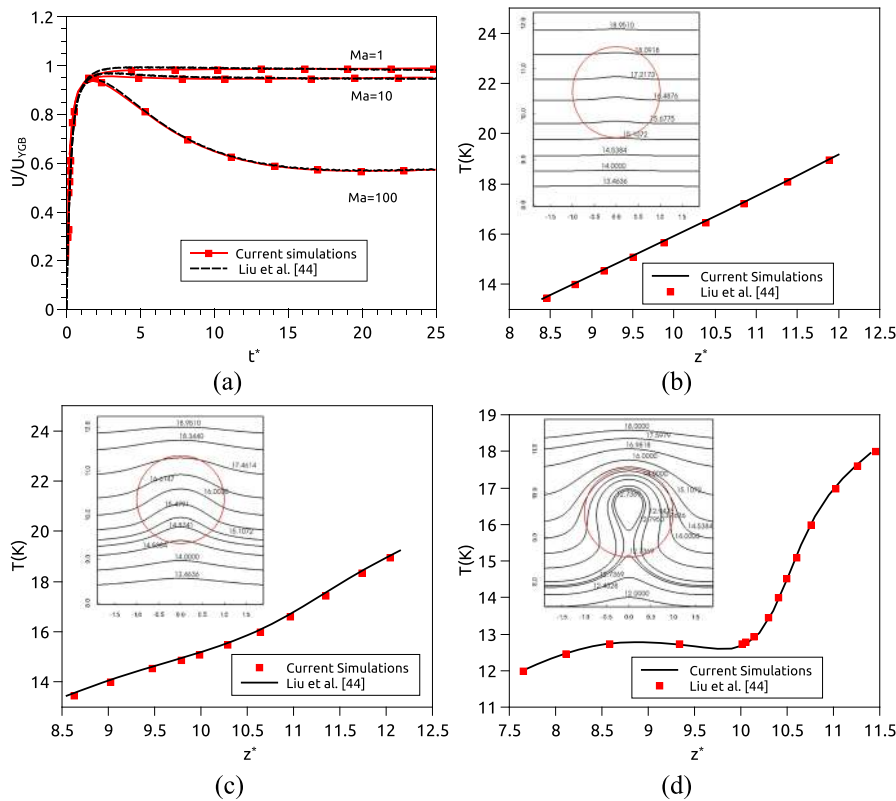


FIG. 3. (a) Temporal evolution of velocity for the case of $Ma = 1, 10, 100$ with comparison to the results predicted by Liu *et al.*⁴⁴ Axial temperature distribution inside the droplet and its near vicinity with comparison to the temperatures predicted by Liu *et al.*⁴⁴ (b) $Ma = 1$, (c) $Ma = 10$, and (d) $Ma = 100$. Isotherms of the corresponding Marangoni number are represented in the inset.

negligible. Studies by Chen *et al.*²⁷ and Mahesri *et al.*³⁰ have shown enhanced hydrodynamic retarding effect due to the proximity of the wall. Though the retardation effect is brought out in the previous studies, the effect of relative droplet size and constriction size on the migration velocity is not clearly discussed. To investigate the retardation of the droplet due to the presence of the wall, the droplet size is varied in a constricted domain of fixed size.

TABLE II. Property ratios corresponding to the experimental studies of Hadland *et al.*¹⁰

Property ratio	ρ_r	μ_r	C_r	k_r
Value	1.88	0.14	0.58	0.47

TABLE III. Grid independence test corresponding to the case of Hadland *et al.*¹⁰ for the case of $Ma = 100$.

Grid size (Cells/ a)	Velocity (U/U_{YGB})	Relative percentage difference (%)
10	0.3957	...
20	0.3777	4.5489
30	0.3743	0.9002
40	0.3732	0.2939
50	0.3728	0.1072

A. Variation of droplet size in a constricted domain

The studies are performed in a computational domain depicted in Fig. 2 which is of length $l = 20a$ and droplet initialised at a distance of $b = 3a$ from the bottom wall. The CS

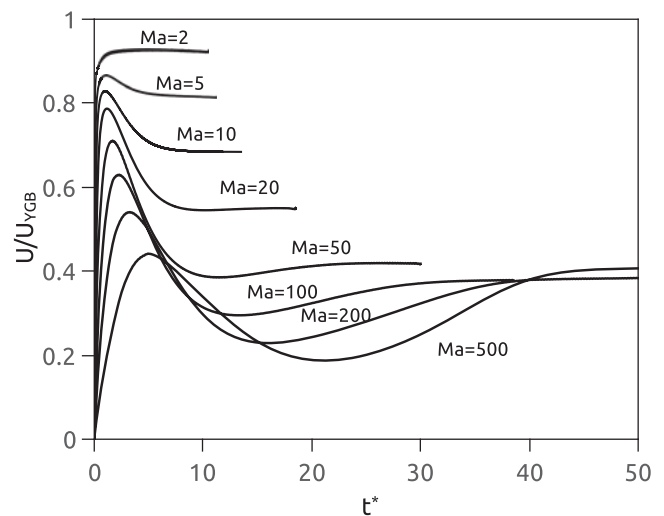


FIG. 4. Temporal evolution of velocity normalized with corresponding U_{YGB} for Marangoni numbers varying between $Ma = 2$ and $Ma = 500$.

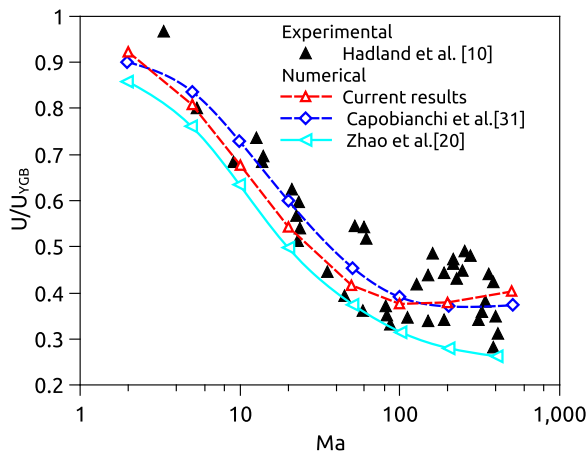


FIG. 5. Comparison of the velocities at steady state obtained from the current numerical studies with the experimentally observed velocities¹⁰ along with the numerically predicted velocities^{20,31} reported previously.

in the schematic defines the constriction size of the domain and for the present study, the value of CS is fixed to be 0.6 which corresponds to a domain whose diameter is 1.67 times the largest considered droplet radius (a) considered. No slip condition for the velocity is applied to all the walls, and the Neumann boundary condition for temperature is applied on the side wall. The temperature at the top and bottom walls are fixed to generate a constant temperature gradient in the

ambient fluid to achieve non-dimensional parametric values of $Ma = 100$ and $Re = 1.2$, corresponding to a droplet of radius a with properties corresponding to the ratios provided in Table II. The droplet radius is varied between $0.3a$ and a , in steps of $0.1a$, which corresponds to ζ varying between 0.3 and 1 in the computational domain. Numerical simulations are performed, and the predicted steady-state velocities corresponding to each radius (ζ) are non-dimensionalized with their respective U_{YGB} velocity values and are plotted in Fig. 6(a). The ratio of velocities (U/U_{YGB}) is observed to decrease with ζ which is similar to the trend reported by Mahesri et al.³⁰ Figure 6(c) shows the isotherm and droplet interface snapshots at $t^* = 96$ corresponding to each value of ζ . The relative droplet positions across the snapshots show a non-monotonic dependence of velocity with ζ unlike the monotonic trend for the normalized velocity U/U_{YGB} , in Fig. 6(a). For the same initial conditions, the Marangoni number (Ma) increases from 9 to 100 as ζ increases from 0.3 to 1. Thus, the monotonic decrease of U/U_{YGB} with ζ is attributed to the convective effects for higher Ma , as shown in Fig. 4. The real effect of ζ on the velocity of migration of the droplet is not captured by U/U_{YGB} . In an attempt to identify a non-dimensionalized parameter which matches the trend of droplet position observed in the snapshots, all the velocities are non-dimensionalized with the velocity scale (U_T) corresponding to the largest droplet radius a . The variation of this parameter U^* with ζ is presented in Fig. 6(a) [refer to Eqs. (9) and (10)]. The value of U^* increases upto $\zeta = 0.6$ and then decreases, matching the variation observed in the snapshots in Fig. 6(c).

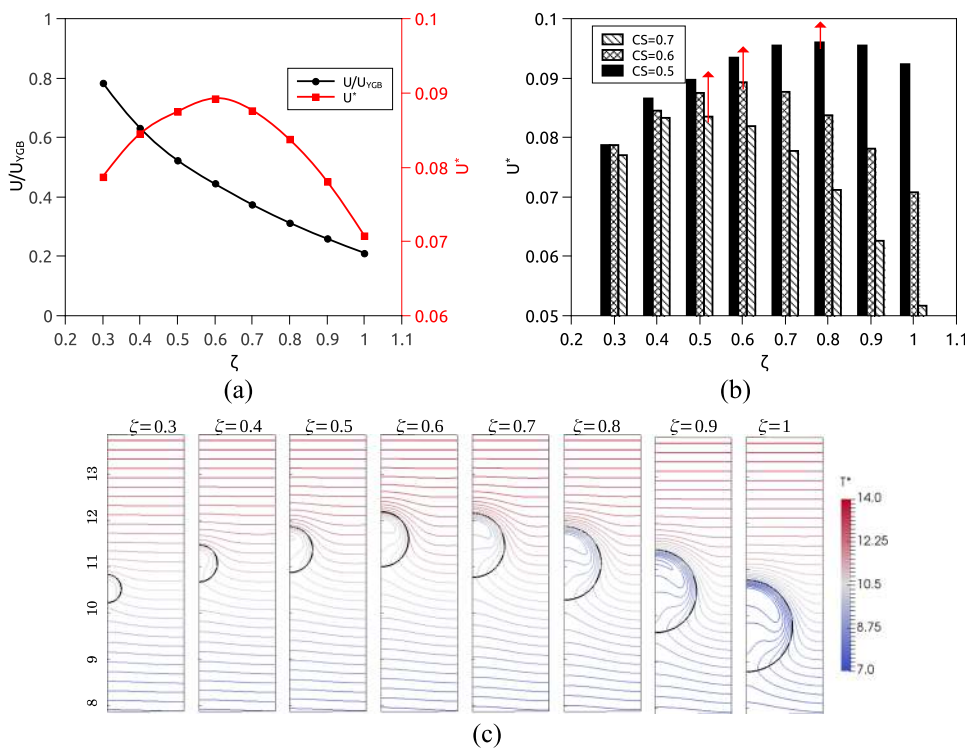


FIG. 6. (a) Variation of non-dimensional velocity U^* and normalized velocity U/U_{YGB} at steady state with droplet size (ζ) in a domain with CS = 0.6. (b) Comparison of non-dimensional velocities at steady state for a single droplet with varying droplet sizes (ζ varied from 0.3 to 1 in step sizes of 0.1) in a domain with fixed CS of 0.5, 0.6, and 0.7, respectively. The arrows in red indicate the location of ζ with maximum velocity for the corresponding CS. (c) Isotherms for different droplet sizes with ζ varying between 0.3 and 1.0 in step sizes of 0.1 in a domain with a fixed constriction of CS = 0.6 at $t^* = 96$.

For coherence, the U_r corresponding to radius a is considered for non-dimensionalization in all the subsequent cases in the present work. To investigate the wall effects in other domains, droplet sizes are varied in domains with $CS = 0.5$ and 0.7 , and the corresponding non-dimensional velocities U^* are plotted in Fig. 6(b) along with the velocities obtained for $CS = 0.6$. It is observed that for all the domains, the U^* and ζ dependence follow similar trends. The value of ζ at which maximum U^* is obtained shifts towards smaller values of ζ with increasing CS .

A force analysis helps in understanding the effect of wall proximity on the velocity of migration. In the present case, the thermocapillary force is the driving force whereas the drag is the resisting force. Chen *et al.*²⁷ estimated the dimensional lift force due to the thermocapillary effect as

$$F_{tc} = -4\pi(\zeta a)^2 \frac{\partial \sigma}{\partial T} \Delta T_\infty \left(\frac{\lambda_m}{(1 + \mu_r)(2 + k_r)} \right), \quad (14)$$

where λ_m is the lift coefficient which factors in the change of interfacial temperature value due to wall proximity. At higher Marangoni numbers, in addition to the wall effects, convection causes changes in the interfacial temperature gradient. Therefore, to accurately estimate the thermocapillary force, $2\zeta a \Delta T_\infty$ is replaced by the interfacial temperature difference (δT_i) obtained from the numerical results in Eq. (14). Since δT_i is taken from the numerical values, Eq. (14) reduces to

$$F_{tc} \approx 2\pi(\zeta a) \frac{\partial \sigma}{\partial T} \delta T_i \left(\frac{1}{(1 + \mu_r)(2 + k_r)} \right). \quad (15)$$

The Reynolds number (based on the droplet velocity) is very small in the present case, and the flow around the droplet can be considered as creeping. Viscous drag is dominant in this regime and varies linearly with droplet velocity. The drag force acting on the droplet can be estimated with an expression similar to that of Chen *et al.*²⁷ as

$$F_D \approx -4\pi\zeta a \mu_c \left(\frac{1 + \frac{3}{2}\mu_r}{1 + \mu_r} \right) \lambda U, \quad (16)$$

where λ is the drag coefficient, and U is the droplet migration velocity. At steady state, the net force acting on the droplet is zero, and the thermocapillary force equals the drag force.

The value of the drag coefficient (λ) is obtained by substituting the steady-state values of interfacial temperature difference (δT_i) and migration velocity (U) in Eqs. (15) and (16), respectively. The thermocapillary force acting on the droplet is non-dimensionalized with the force acting on a droplet of radius a migrating with no convective and wall effects in the ambient fluid with a temperature gradient ΔT_∞ . The reference force is given by

$$F_{ref} = -4\pi a^2 \frac{\partial \sigma}{\partial T} \Delta T_\infty \left(\frac{1}{(1 + \mu_r)(2 + k_r)} \right). \quad (17)$$

The non-dimensionalized thermocapillary force (F_{tc}/F_{ref}) and the drag coefficient (λ) corresponding to each droplet size (ζ) in domains with $CS = 0.5, 0.6,$ and 0.7 are plotted in Fig. 7(a).

It is observed that both the dimensionless thermocapillary force (F_{tc}/F_{ref}) and the drag coefficient (λ) increase with the size of the droplet (ζ), for a domain with fixed CS . At fixed droplet size (ζ), the thermocapillary force is observed to slightly increase or remain constant, whereas the drag coefficient (λ) increases with an increase in CS . The rate of change of λ with ζ is also observed to increase with CS indicating a more significant effect of wall proximity on droplet migration. At a fixed domain size (CS), for the smallest droplet ($\zeta = 0.3$), both the thermocapillary force and the drag coefficient are smaller resulting in smaller migration velocity. As the droplet size (ζ) increases, the interfacial flow becomes stronger due to larger δT_i and, as a consequence, the thermocapillary force increases. However, at close proximity of the wall, the drag coefficient also increases rapidly. The combined effect of the rise in the thermocapillary force (F_{tc}/F_{ref}) and the drag coefficient (λ) gives rise to a maximum value for the velocity (U^*) for an intermediate value of the drop size parameter (ζ) as observed in Fig. 6(a). After this particular value of ζ , the increase in λ outgrows the increase in the thermocapillary force (F_{tc}/F_{ref}) thereby causing, a decrease of velocity. Hence, despite the fact that a droplet with $\zeta = 1.0$ has a larger F_{tc}/F_{ref} , the larger value of λ makes the droplet move with a lower migration velocity [Fig. 6(b)]. The increase in λ with CS for a fixed ζ makes the wall effects to be felt at a smaller value of ζ . This increase in λ results in a shift of maximum velocity towards a smaller value of ζ with an increase in CS as observed in Fig. 6(b). Larger droplet sizes (ζ) are observed to have an

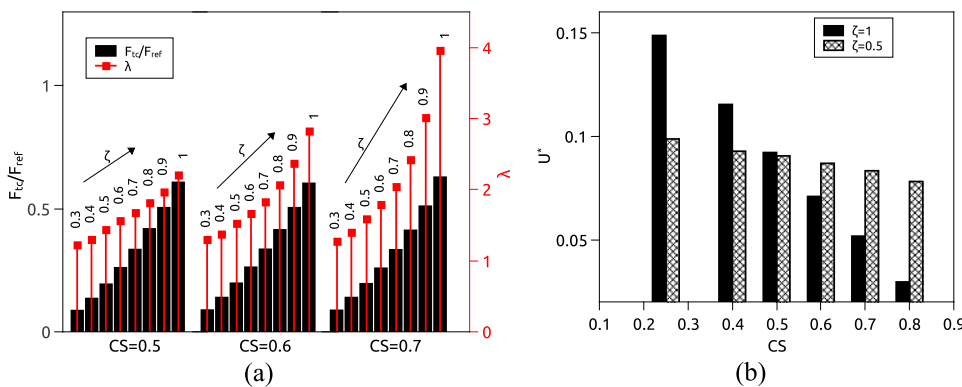


FIG. 7. (a) Non dimensional thermocapillary force (F_{tc}/F_{ref}) and drag coefficient (λ) corresponding to each droplet of size (ζ) migrating in a domain with $CS = 0.5, 0.6,$ and 0.7 , respectively. The number on the column corresponds to the droplet size (ζ). (b) Comparison of velocities at steady state obtained for thermocapillary migration of droplets with $\zeta = 1$ and $\zeta = 0.5$ in domains with CS varying between 0.25 and 0.8 .

increased effect of drag due to their proximity to the wall. For instance, 44% reduction in the droplet velocity is observed for the droplet with $\zeta = 1$, whereas only a 2% reduction is observed for $\zeta = 0.3$ as CS increases from 0.5 to 0.7.

To investigate the effect of constriction size (CS) on the migration velocity on a droplet of fixed size, size parameter values of $\zeta = 1$ and $\zeta = 0.5$ are considered with CS varying between 0.25 and 0.8, and the predicted non-dimensional steady-state velocities are plotted in Fig. 7(b). It is seen that for a droplet with fixed ζ , the value of U^* decreases with CS. It is also observed that the droplet with $\zeta = 0.5$ travels faster than a droplet with $\zeta = 1$ for domains with $CS > 0.5$, whereas it is slower for $CS \leq 0.5$. The observed effect is attributed to the proximity of the interface of the droplet to the wall which alters the drag coefficient (λ) as shown in Fig. 7(a). The instantaneous thermal field features for droplets sizes with $\zeta = 1$ and $\zeta = 0.5$ for domains with different constriction sizes (CS) at $t^* = 96$ are shown in Figs. 8(a) and 8(b). The right half of each plot depicts the instantaneous isothermal contours, while the left half illustrates the dimensional temperature deviation contours, from the initially imposed temperature field with a uniform temperature gradient. The temperature deviation contours indicate the effect of droplet's internal convection on the thermal field within the droplet. More importantly, the size of the thermal wake behind the migrating droplet is significantly affected by the drop size as well as the constriction size. For a smaller constriction size (CS), the thermal wake length is relatively larger. Also, the thermal wake length increases with the drop size. In other words, larger droplets have relatively larger wake lengths, at a fixed constriction size. The variations observed in the thermal wake length of a migrating droplet

have great significance in the case of multi-droplet thermocapillary migration. In particular, the migration of the trailing droplet will be immensely affected by the temperature variation in the thermal wake of the leading droplet. Since wake features are influenced by the size of droplet and domain constriction, migration dynamics of the trailing droplet is also expected to be strongly influenced by the parameters of ζ and CS.

It can be concluded from the present study that with the introduction of a wall, the temperature and velocity evolutions get affected, and in some cases, the larger droplet travels slower than, the smaller droplet. The observed changes significantly affect the interactions of droplets when wall effects are also present. With this background, Sec. V presents studies on two-droplet interactions in constricted domains.

V. THERMOCAPILLARY MIGRATION OF TWO INTERACTING DROPLETS

Other than the proximity to the wall, the presence of another fluid particle can lead to momentum and thermal interactions which eventually affect the migration dynamics of both the fluid particles. A special case of such droplet interactions is considered where one droplet is followed by another and the two are aligned along the temperature gradient. In this configuration, if the leading droplet is faster, the interaction of two droplets does not occur since the leading droplet outruns the trailing one. On the other hand, if the trailing droplet is faster, the two droplets will interact. Previous studies,^{21,40} considered unbounded domains where the larger droplet is always faster and hence studies were

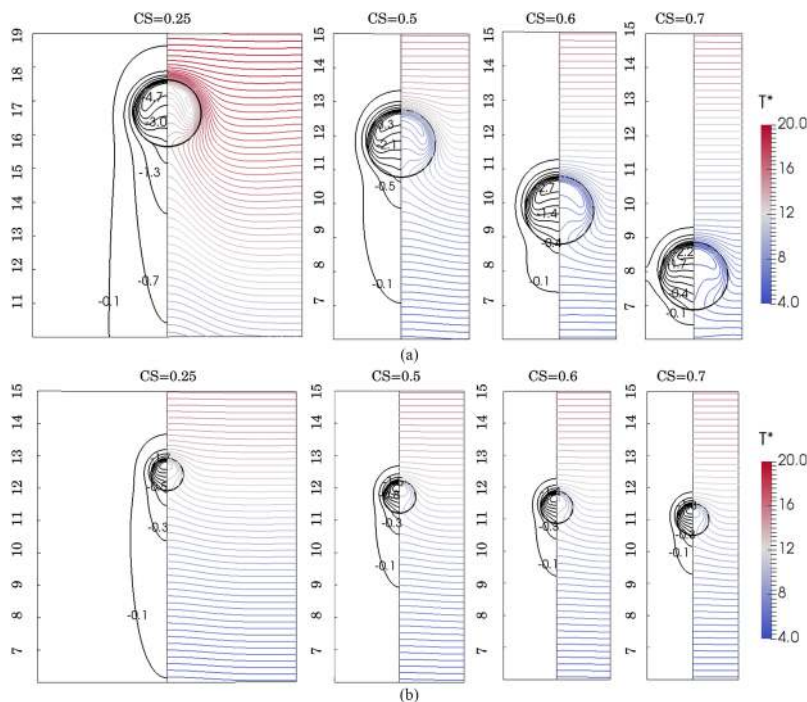


FIG. 8. Contours of temperature perturbation (left) and isotherms (right) at $t^* = 95$ for a single droplet with (a) $\zeta = 1$ and (b) $\zeta = 0.5$ migrating in different constricted domains with CS varying between 0.25 and 0.7.

performed only for the configuration in which the larger droplet follows the smaller one. From the results in Sec. IV, it is seen that the smaller droplet may be faster than the larger one in constricted domains. Thus, an alternative configuration of interaction, in which the smaller droplet follows the larger one, is possible when droplets are migrating in constricted domains. Before studying droplet interaction in constricted domains, the solver is validated with the numerical predictions of thermocapillary droplet interaction by Yin and Li.⁴⁰

A. Two interacting droplets in aligned arrangement without wall effects—Validation

In the numerical test case studied by Yin and Li,⁴⁰ droplet interactions between a leading droplet of radius $0.5a$ and a trailing droplet of radius a is considered in a computational domain of radius $4a$ and length $20a$. The computational domain used for the validation is shown in Fig. 9. An axisymmetric domain of length $20a$ and radius a/CS is considered with the following boundary conditions. No slip condition for velocity is applied to all the walls. The Neumann condition on the lateral wall and the Dirichlet condition on the top and bottom walls are applied for temperature to impose a one-dimensional temperature gradient. The droplet of radius

$a * \zeta_2$ is initialized at a distance of $3a$ from the bottom wall, and the droplet of radius $a * \zeta_1$ is initialized at a distance of S_0 from the center of former droplet along the axis of symmetry. Here ζ_1 and ζ_2 are droplet size parameters, which vary between 0 and 1. The constriction size (CS) of the domain also varies between 0 and 1. The domain considered in the validation test case corresponds to the computational domain with $\zeta_1 = 0.5$, $\zeta_2 = 1$, $S_0 = 2.5a$ and $CS = 0.25$. For fluid properties, the property ratio values given in Table II are considered, along with the non-dimensional numbers of $Ma = 100$, $Re = 1.2$, and $Ca = 0.05$. Numerical simulations are performed and the temporal evolutions of the droplet migration velocities are plotted in Fig. 10(a). Velocity evolution with time for migration of the single droplet with $\zeta = 1$ and $\zeta = 0.5$ is also plotted in Fig. 10(a) for comparison. Figure 10(b) shows the temporal evolution of the separation distance (S) predicted by the present

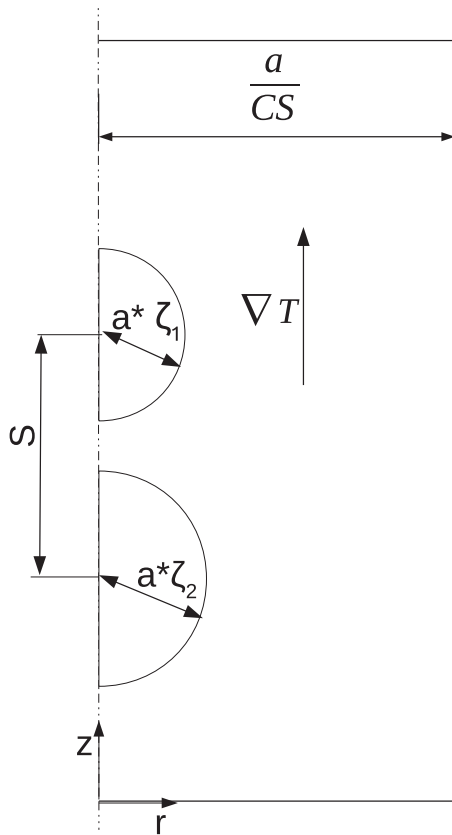


FIG. 9. Schematic of the computational domain for studying the thermocapillary droplet migration of two droplets of different sizes in an aligned configuration.

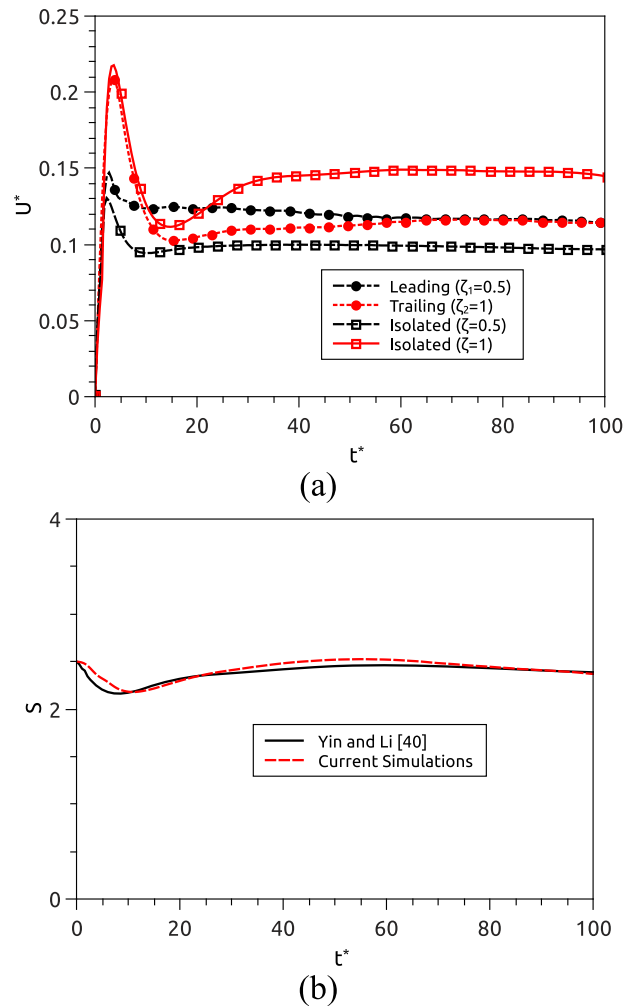


FIG. 10. (a) Temporal evolution of velocity of isolated droplet and interaction cases of the leading droplet with $\zeta_1 = 0.5$ and the trailing droplet with $\zeta_2 = 1$ migrating in the domain with $CS = 0.25$. (b) Temporal evolution of the separation distance and comparison with numerical predictions from Yin and Li.⁴⁰

code and the corresponding predictions of Yin and Li.⁴⁰ It is observed that the two sets of results corroborate well. The results show that the droplets do not coalesce but instead migrate together with a steady state separation distance. It is seen in Fig. 10(a) that an isolated droplet with $\zeta = 1$ travels faster than the an isolated droplet with $\zeta = 0.5$. When they migrate together, the droplets are expected to coalesce, but it is observed that both droplets travel at the same migration velocity eventually. The droplet with $\zeta_1 = 0.5$ migrates faster, whereas the droplet with $\zeta_2 = 1$ migrates slower than the single droplet migration velocity. This change in migration behaviour of the two droplets is attributed to thermal wake interaction. The leading droplet leaves thermal wake (a perturbed temperature field in the ambient) and when the trailing droplet moves into this region the effective temperature gradient along its interface is reduced, thus slowing down the droplet. The clustered isotherms at the top portion of the trailing droplet cause an increase in the temperature gradient across the interface of the leading droplet resulting in its faster migration. The slowing down of the trailing droplet and speeding up of the leading droplet has a net effect of both the droplets migrating together with an equilibrium separation distance at later times. The two droplets' thermocapillary migration has been validated for an unbounded domain, and hence thermocapillary droplet interactions in confined domains are now considered.

B. Thermocapillary migration of two droplets in a constricted domain

The proportionality between the droplet radius and migration velocity observed in an unbounded domain is not valid in the presence of a constriction. This allows the possibility that a larger droplet does not travel faster than a smaller droplet. To study the interaction effects inside a constricted domain, two configurations are considered one in which the larger droplet follows the smaller (referred to as configuration SB) and another in which the smaller droplet follows the larger (referred to as configuration BS). In the present study, the two droplets considered have sizes $\zeta = 1$ and 0.5 . In configuration

SB, the leading droplet has the size of $\zeta_1 = 0.5$ and the trailing droplet has the size of $\zeta_2 = 1$. In the configuration BS, the leading droplet has the size of $\zeta_1 = 1$ and the trailing droplet has the size of $\zeta_2 = 0.5$. The fluid properties correspond to property ratios listed in Table II along with non-dimensional number values of $Ma = 100$, $Re = 1.2$, and $Ca = 0.05$ calculated with respect to the reference radius a . The initial separation distance is set as $S_0 = 2.5a$ in all the simulations. Numerical simulations are performed with both the configurations (BS and SB) in the domain shown in Fig. 9 with CS values ranging from 0.25 to 0.8. The temporal evolution of the droplet separation distance (S) for different CS values in both the configurations are shown in Fig. 11. The isotherms corresponding to each CS at $t^* = 95$ (approaching steady state) are shown in Fig. 12. The relative position of the droplets in Fig. 12 gives an overall picture of the droplet interactions. It is seen from Figs. 11 and 12 that the influence of CS on the interaction dynamics is opposite in the two configurations. For the configuration SB [Fig. 11(a)], the separation distance (S) achieves a steady state for $CS \leq 0.5$ and increases monotonically with time for $CS > 0.5$. On the other hand, for BS configuration, the separation distance (S) achieves a steady state for $CS > 0.5$ and increases monotonically with time for $CS \leq 0.5$ as seen in Fig. 11(b). The observed dependence of interaction on CS is explainable in terms of the behaviour of single droplet velocity in constricted domains, as seen in Fig. 7(b). For domains with $CS \leq 0.5$, the droplet with $\zeta = 1$ always travels faster than the droplet with $\zeta = 0.5$. With an increase in CS, the large drag coefficient (λ) resulting due to the proximity of the wall makes the droplet with $\zeta = 1$ move with less velocity than the droplet with $\zeta = 0.5$. In BS configuration, for domains with $CS \leq 0.5$, the droplet with $\zeta_1 = 1$ travels faster, whereas in configuration SB, the droplet with $\zeta_1 = 0.5$ travels faster for domains with $CS > 0.5$. Hence in both configurations, the faster leading droplet outruns the trailing droplet causing a monotonically increasing separation distance proportional to the difference of velocities as observed in Figs. 11(a) and 11(b). For the domains with $CS \leq 0.5$ in configuration SB and the domains with $CS > 0.5$ in configuration BS, interaction occurs due to the leading droplet migrating with lower velocity. The interaction reduces

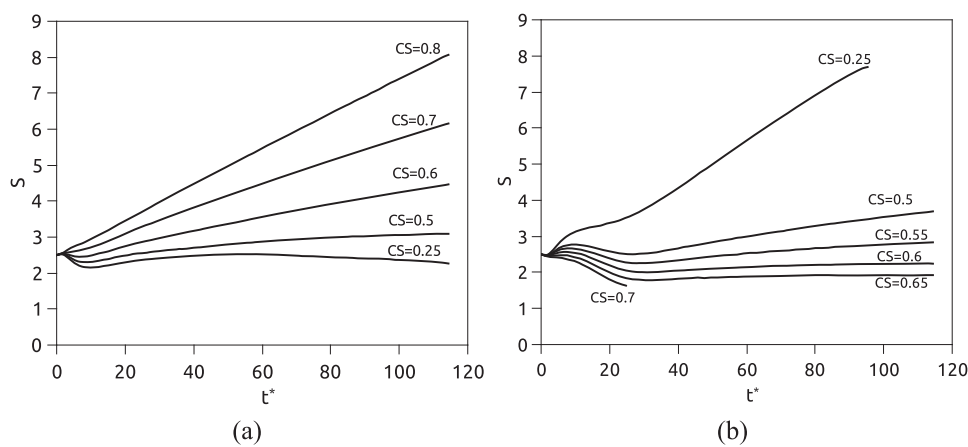


FIG. 11. Temporal evolution of separation distance (S) between two droplets with migrating together in domains with CS varying between 0.25 and 0.8. (a) SB configuration. (b) BS configuration.

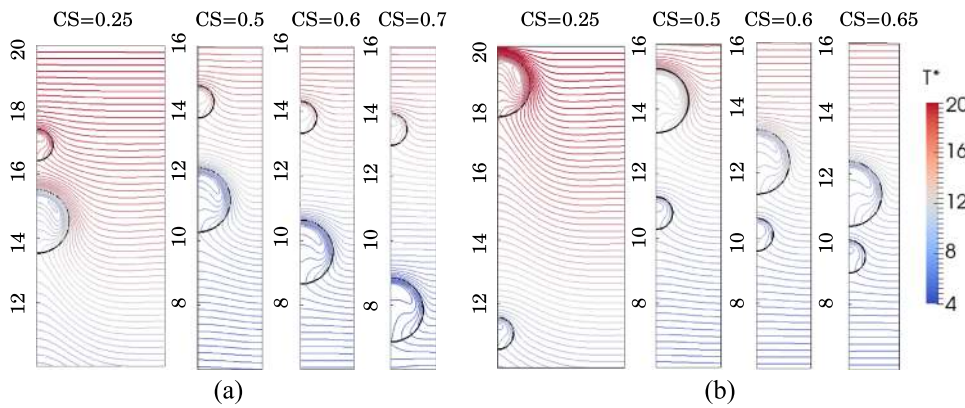


FIG. 12. Isotherms of two droplets ($\zeta_1 = 1$ and $\zeta_2 = 0.5$) migrating with interaction in domains at $t^* = 95$ with CS varying between 0.25 and 0.7. (a) SB configuration. (b) BS configuration.

the speed of the trailing droplet and increases the speed of the leading droplet due to thermal wake interactions. This results in a steady state separation distance as discussed earlier. Droplet interactions in SB configuration have been extensively studied in previous studies.^{21,40} Hence, interactions in this configuration will not be discussed further. From Fig. 11(b), it is seen that the steady state separation distance decreases with constriction size (CS) in configuration BS. The observed behaviour is attributed to the diminishing thermal wake of the leading droplet, caused due to the increase in CS [refer to Fig. 8(a)]. Hence, in this case, thermal wake interactions occur only at reduced separation distance. After a certain CS, the diminishing thermal wake interactions may not be able to reduce the droplet velocity to less than or equal to that of the leading droplet, thereby resulting in droplet coalescence. For the present study, coalescence is observed at CS = 0.7, and hence, the evolution of separation distance (S) is partially tracked in Fig. 11(b). The coalescence may actually happen at a larger value of CS; however, the numerical method adopted in the present study leads to a merger of droplet interface when they are separated by 10 grids or less.

As steady state separation distance is observed for a domain with CS = 0.6, further simulations are carried out in this domain to understand the influence of the initial separation distance, trailing droplet size and Marangoni number on droplet interactions and the separation distance.

C. Effect of initial separation distance

In Sec. V B, the initial separation distance was set to $S_0 = 2.5a$ for droplets travelling in configuration BS. To understand the effect of initial separation distance on the interaction of droplets, numerical simulations are performed additionally for the separation distances of $S_0 = 2a$ and $3a$ in a domain with CS = 0.6, $\zeta_1 = 1$, $\zeta_2 = 0.5$ keeping all the initial and boundary conditions same as in the previous case.

Figure 13(a) shows the temporal evolution of the dimensionless separation distance (S) associated with different initial separation distances (S_0). It is observed that the predicted steady state separation distance (S_F) is independent of S_0 . Temporal evolution of velocity for leading ($\zeta_1 = 1$) and trailing ($\zeta_2 = 0.5$) droplets for various initial separation distances

is plotted in Figs. 13(c) and 13(d), respectively. The velocity evolution corresponding to the single droplet migration of the leading and trailing droplets are also included for comparison. The leading droplet ($\zeta_1 = 1$) travels with almost the same velocity as in the case of a single droplet. The evolution of the velocity is also observed to be independent of S_0 . The trailing droplet ($\zeta_2 = 0.5$), which is supposed to be faster in the domain with CS = 0.6, decelerates to the leading droplet ($\zeta_1 = 1$) velocity at steady state. Furthermore, the temporal evolution of velocity for the trailing droplet is observed to vary with S_0 . The magnitude of temperature difference (δT_i) across the trailing droplet can be related to the thermocapillary driving potential and therefore can be used to understand the velocity evolution better. The interfacial temperature difference (δT_i) for both leading and trailing droplets is plotted in Fig. 13(b). The interfacial temperature difference evolution for the case of migration of single droplet is also included in the corresponding plots. The initial decrease of temperature difference across the trailing droplet interface (for all tested S_0) is the same as when it is moving as a single droplet. This is followed by an increase in the temperature difference which is only observed to be prominent for the case of two-droplet migration. This increase in temperature difference is manifested as a second acceleration in the velocity evolution and the trailing droplet ($\zeta_2 = 0.5$) moves closer towards the leading droplet ($\zeta_1 = 1$) until it reaches the thermal wake. The thermal wake interactions result in a decrease of interfacial temperature difference which slows down the droplet. The point of inception of the deceleration or thermal wake interaction depends on the initial separation distance. For the case with $S_0 = 2a$, the droplet interacts with the thermal wake early and results in an early deceleration whereas, for the case with $S_0 = 3a$, deceleration starts relatively later. Also, the magnitude of deceleration increases with the closeness to the leading droplet ($\zeta_1 = 1$) such that the trailing droplet ($\zeta_2 = 0.5$) is pushed out of thermal wake zone, as observed for the case with $S_0 = 2a$. Then, the trailing droplet ($\zeta_2 = 0.5$) again accelerates to reach a steady state velocity such that thermal wake interaction results in an unchanged interfacial temperature gradient. For larger initial separation distance ($S_0 = 3a$), the deceleration of the trailing droplet ($\zeta_2 = 0.5$) is not prominent as it is farther away and hence the droplet

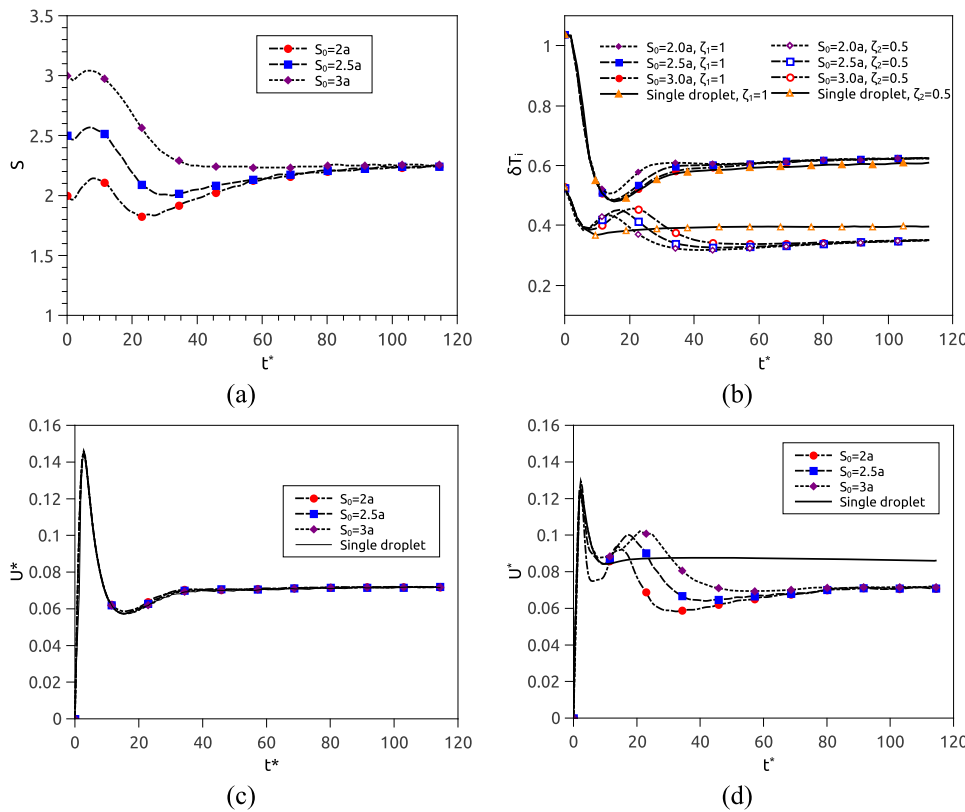


FIG. 13. Effect of variation of initial separation distance (S_0) between the droplets with $\zeta = 0.5$ and $\zeta = 1$ migrating in BS configuration in a computational domain with $CS = 0.6$ on (a) temporal evolution of separation distance (S), (b) temporal evolution of temperature difference along the interface for both the droplets, (c) temporal evolution of velocity of the leading droplet ($\zeta_1 = 1$), and (d) temporal evolution of velocity of the trailing droplet ($\zeta_2 = 0.5$). Corresponding single drop results are also added for comparison.

decelerates to attain the steady state velocity directly. For an intermediate initial separation distance ($S_0 = 2.5a$) a slight final acceleration is observed. The temperature difference across the interface of the leading droplet ($\zeta_1 = 1$) increases slightly as compared with that of single droplet migration and the evolution of the temperature difference is also noted to change with initial separation. The leading droplet velocity and its evolution appear to be uninfluenced by a change in the temperature difference. To investigate this further, the thermocapillary force and drag coefficient are evaluated using Eqs. (15) and (16), and they are listed in Table IV. The thermocapillary force and drag coefficients for the case of single droplet migration are also included in the table.

The drag coefficient (λ) is observed to increase for both leading and trailing droplets when droplets are migrating together, indicating the increased effect of drag. The

thermocapillary force (F_{tc}/F_{ref}) is observed to increase for the leading droplet and decrease for the trailing droplet as expected, due to interaction. The increase in thermocapillary force (F_{tc}/F_{ref}) is balanced by the increase in drag coefficient (λ) making the leading droplet to travel with a velocity close to that of the single droplet case. For trailing droplet, the decrease in thermocapillary force (F_{tc}/F_{ref}) accompanied by an increase in drag coefficient (λ), makes the droplet travel at a lower velocity compared to the single droplet case, thus preventing coalescence. The convergence of final separation distance (S_F) to the same value for various initial separation distances (S_0) in configuration BS clearly shows that it is independent of initial separation and is governed only by the dynamic thermal wake interactions.

D. Effect of radius of trailing droplet

To study the effect of trailing droplet radius on the interaction, the value of ζ_1 is set to 1 while the value of ζ_2 is varied between 0.3 and 1. Numerical simulations are performed in the domain with $CS = 0.6$ keeping boundary conditions same as in the previous cases and non-dimensional number values of $Ma = 100$, $Re = 1.2$, $Ca = 0.05$.

For each trailing droplet size considered, it is observed that a steady state separation distance is achieved. The variation of steady state separation distance (S_F) is plotted with ζ_2 in Fig. 14. It is observed that the value of S_F decreases up to a certain ζ_2 and then increases. Snapshots in Fig. 15 show

TABLE IV. Non-dimensionalized thermocapillary force (F/F_{ref}) and drag coefficient (λ) of droplets migrating together in an aligned configuration with $\zeta_1 = 1$ and $\zeta_2 = 0.5$ in a domain with $CS = 0.6$ and comparison with single droplet values.

	Leading ($\zeta_1 = 1$)		Trailing ($\zeta_2 = 0.5$)	
	F_{tc}/F_{ref}	λ	F_{tc}/F_{ref}	λ
Single droplet	0.67	2.822	0.219	1.525
Interacting droplet	0.682	2.855	0.194	1.622

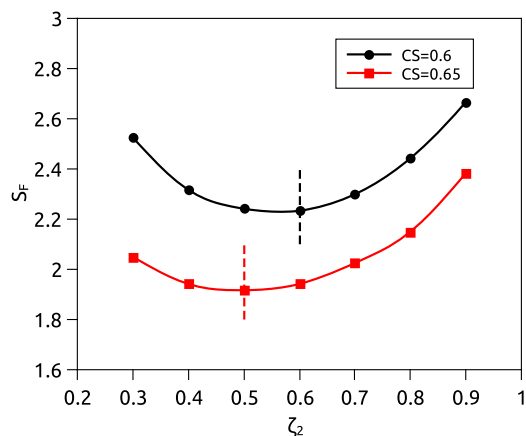


FIG. 14. Comparison of separation distances at steady state for varying trailing droplet sizes ($\zeta_2 = 0.3\text{--}0.9$) when droplets are migrating with leading droplet ($\zeta = 1$) in BS configuration in a domain with CS = 0.6 and CS = 0.65. The dashed line represents the minimum separation distance at steady state for corresponding CS.

the isotherms and droplet interfaces at $t^* = 96$ obtained for different trailing droplet sizes (ζ_2 varying between 0.3 and 0.9). The relative distance between the droplets and the isotherms in each of the snapshots shed some insight into the dynamics of the interactions. The non-monotonic dependence of S_F with ζ_2 can be attributed to the compounding effect of thermal wake and wall induced drag on the trailing droplet. To verify whether a similar phenomenon occurs for other constriction sizes, numerical simulations are also performed by varying the trailing droplet size in the domain with CS = 0.65. The variation of final steady state separation distance (S_F) with ζ_2 is plotted in Fig. 14. In this case too, the similar phenomenon of decrease followed by increase of S_F is observed with trailing droplet size. The minimum of S_F is observed to shift towards the smaller droplet size with increase in CS. The observed shifting of the minimum S_F with increase towards smaller ζ_2 is similar to the phenomenon observed for single droplet migration velocity where velocity maxima shifts towards the smaller value of ζ with an increase in CS.

This study on the effect of trailing droplet radius brings out the complexity and interdependence of thermal and momentum evolutions in thermocapillary migration. It also shows that the presence of the wall, in addition to increasing drag force, causes changes in isotherm evolution, as well as the interaction dynamics between two droplets.

E. Effect of Marangoni number

Numerical studies are performed by varying the Marangoni number between 50 and 150, in a computational domain with CS = 0.6 for droplets with $\zeta_1 = 1$ and $\zeta_2 = 0.5$ in the configuration of BS. The initial separation distance and Capillary number are set to $S_0 = 2.5a$ and $Ca = 0.05$ respectively, for all the cases discussed here.

The temporal evolution of the separation distance for different Marangoni numbers is plotted in Fig. 16(a). It is seen that the separation distance approaches a steady state value for all the cases considered. The final separation distance (S_F) is observed to increase with Marangoni number. The increase of S_F with the Marangoni number is attributed to the strong thermal wake interactions. The change of Marangoni number changes the temperature evolution in both the droplet and the ambient fluid as shown in the snapshots of Fig. 16(b). The strength of thermal wake of the leading droplet also increases with Marangoni number, due to increased convective effects. To analyse the effect of thermocapillary interaction on the separation distance, further analysis is performed on the forces acting on the droplets.

The thermocapillary force values for both leading and trailing droplets at steady state for different Marangoni numbers are calculated using Eq. (15) and non-dimensionalized with F_{ref} [Eq. (17)] corresponding to $Ma = 100$ and tabulated in Table V. The drag coefficients are also tabulated which are calculated by equating the thermocapillary force [Eq. (15)] to the drag force [Eq. (16)]. The values of U/U_{YGB} of the leading droplet are also listed in the Table. The increase of U/U_{YGB} for $Ma > 100$ as seen in Fig. 5 is not observed in constricted domain (CS = 0.6) due to the reduced convection inside the droplet compared to the case of migration of droplet in an unbounded domain. It is observed that the drag coefficient (λ) slightly increases with Ma and since both the droplets experience increased drag, its effect

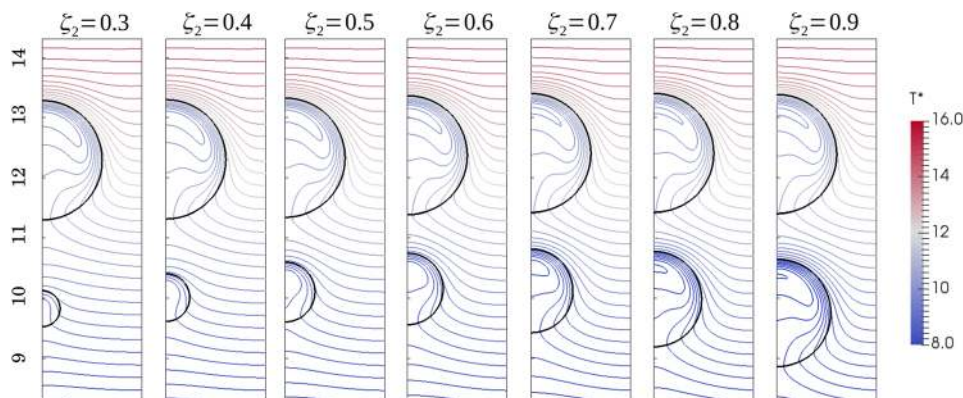


FIG. 15. Isotherms at $t^* = 96$ for droplets migrating in BS configuration with constant leading droplet size of $\zeta_1 = 1$ and different trailing droplet sizes with ζ_2 varying between 0.3 and 0.9.

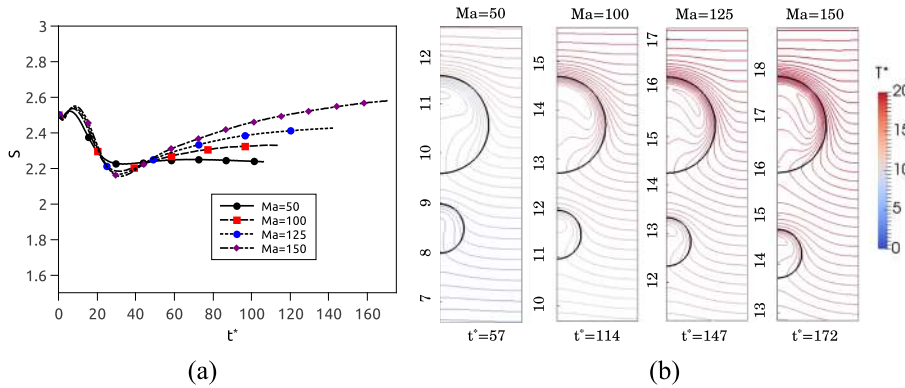


FIG. 16. Effect of Marangoni number for two droplets migrating in BS configuration ($\zeta_1 = 1, \zeta_2 = 0.5, CS = 0.6$). (a) Temporal evolution of separation distance (S). (b) Isotherms.

on the separation distance (S) can be assumed to be minimal (Table V). The non-dimensional thermocapillary force for both the droplets increases with the Marangoni number, as larger temperature gradients are present in the ambient fluid at higher Marangoni numbers. But the magnitude of increase in the thermocapillary force of the trailing droplet is smaller in comparison to that of the leading droplet. The net effect gives rise to higher thermal wake interactions at higher Marangoni numbers. The change in the thermal evolution of the rear droplet coupled with the enhanced thermal wake strength of leading droplet results in larger separation distance.

The evolution of separation distance for $Ma = 50$ [Fig. 16(a)] is similar to that for a larger ($S_0 = 3a$) initial separation distance [Fig. 13(a)]. Also, the evolution of separation distance for $Ma = 150$ [Fig. 16(a)] is similar to that for a smaller ($S_0 = 2a$) initial separation distance [Fig. 13(a)]. It appears that the interaction in the case of a larger thermal wake is similar to that of a smaller initial separation distance and vice versa. At a fixed initial separation distance, for a larger thermal wake of the leading droplet, the distance to be travelled by the trailing droplet to interact with the wake is shorter, whereas, for a smaller thermal wake, it is longer. This shows that the separation distance evolution, shown in Fig. 16(a), is also indicative of the strength of thermal wake of the leading droplet due to the change in Marangoni number.

The decrease in S_F with decrease in the Marangoni number suggests that droplets will coalesce at smaller Marangoni number due to lack of thermal wake interactions. The observed variation in the evolution of separation distance and the final separation distance (S_F) variation with the Marangoni number show the dominant effect of Ma in deciding the

TABLE V. Effect of Marangoni number on dimensionless thermocapillary force (F/F_{ref}) and drag coefficient (λ) for BS configuration ($\zeta_1 = 1, \zeta_2 = 0.5, CS = 0.6$).

Marangoni number (Ma)	U/U_{YGB}	Leading ($\zeta_1 = 1$)		Trailing ($\zeta_2 = 0.5$)	
		F_{tc}/F_{ref}	λ	F_{tc}/F_{ref}	λ
50	0.2568	0.389	2.668	0.111	1.518
100	0.2948	0.682	2.855	0.194	1.622
125	0.1947	0.836	2.954	0.232	1.627

mode of interaction for droplets migrating in constricted domains.

VI. CONCLUSIONS

The thermocapillary migration dynamics of single and two confined droplets aligned in the direction of the temperature gradient are studied numerically using an OpenFOAM based two-phase solver. The predictions of the code are validated with numerical and experimental results available in the literature.

The effects of droplet size for a domain of fixed constriction size on single droplet migration are simulated first. The droplet migration velocity is observed to have non-monotonic dependence with velocity maximum at an intermediate radius value. Also, the velocity maximum shifts towards smaller radii with an increase in the domain constriction size. Furthermore, for some constricted domains and certain combinations of droplets size, it is observed that a smaller droplet moves faster than a larger droplet. These are attributed to changes in the interfacial flow due to temperature difference along the drop surface and the drag force on the droplet in the presence of a wall. In case of migration of two droplets in the direction of the temperature gradient, interactions can happen when the trailing droplet moves faster than the leading one. In unbounded domains, larger droplets travel faster and hence interactions are known to occur only in the case of a smaller droplet followed by the larger. The relative slowdown of the larger drop in constricted domains reveals a possibility of another interaction configuration in which smaller droplet follows the larger one. Numerical simulations, in such configuration, showed that the droplets interact beyond a certain constriction size ($CS > 0.5$ in the present study). For moderate constriction sizes ($0.7 > CS > 0.5$), the droplets follow each other with a constant separation distance after reaching a steady state velocity, and for higher constriction sizes they tend to coalesce. Further studies reveal that, for non-coalescing droplets, the steady state separation distance is independent of the initial separation distance for a given Marangoni number. However, it is found to vary non-monotonically with the trailing droplet radius. The separation distance is observed to increase with the Marangoni number. These results highlight the significance of wall effects on droplet migration and interaction

behaviour between multiple droplets. The results will be applicable for the design and analysis of systems such as microfluidic platforms, heat pipes, etc., where droplet migration plays an important role.

REFERENCES

- ¹L. Zhang, J. Aoki, and B. G. Thomas, "Inclusion removal by bubble flotation in a continuous casting mold," *Metall. Mater. Trans. B* **37**, 361–379 (2006).
- ²E. Alm eras, F. Risso, V. Roig, S. Cazin, C. Plais, and F. Augier, "Mixing by bubble-induced turbulence," *J. Fluid Mech.* **776**, 458–474 (2015).
- ³G. M. Homsy, "Thermocapillary migration of long bubbles in cylindrical capillary tubes," *Phys. Fluids* **15**, 308–314 (2003).
- ⁴B. Sobac, A. Rednikov, S. Dorbolo, and P. Colinet, "Self-propelled Leidenfrost drops on a thermal gradient: A theoretical study," *Phys. Fluids* **29** (2017).
- ⁵J. Kim, "Review of nucleate pool boiling bubble heat transfer mechanisms," *Int. J. Multiphase Flow* **35**, 1067–1076 (2009).
- ⁶S. Das, S. Manda, and S. Chakraborty, "Cross-stream migration of a surfactant-laden deformable droplet in a Poiseuille flow," *Phys. Fluids* **29** (2017).
- ⁷S. Das and S. Chakraborty, "Influence of complex interfacial rheology on the thermocapillary migration of a surfactant-laden droplet in Poiseuille flow," *Phys. Fluids* **30** (2018).
- ⁸M. Meyyappan, W. R. Wilcox, and R. Subramanian, "The slow axisymmetric motion of two bubbles in a thermal gradient," *J. Colloid Interface Sci.* **94**, 243–257 (1983).
- ⁹N. O. Young, J. S. Goldstein, and M. J. Block, "The motion of bubbles in a vertical temperature gradient," *J. Fluid Mech.* **6**, 350–356 (1959).
- ¹⁰P. H. Hadland, R. Balasubramanian, G. Wozniak, and R. S. Subramanian, "Thermocapillary migration of bubbles and drops at moderate to large Marangoni number and moderate Reynolds number in reduced gravity," *Exp. Fluids* **26**, 240–248 (1999).
- ¹¹R. L. Thompson, K. J. Dewitt, and T. L. Labus, "Marangoni bubble motion phenomenon in zero gravity," *Chem. Eng. Commun.* **5**, 299–314 (1980).
- ¹²J. R. Carruthers and L. R. Testardi, "Materials processing in the reduced-gravity environment of space," *Annu. Rev. Mater. Sci.* **13**, 247–278 (1983).
- ¹³R. Balasubramanian and A.-T. Chai, "Thermocapillary migration of droplets: An exact solution for small marangoni numbers," *J. Colloid Interface Sci.* **119**, 531–538 (1987).
- ¹⁴H. Haj-Hariri, A. Nadim, and A. Borhan, "Effect of inertia on the thermocapillary velocity of a drop," *J. Colloid Interface Sci.* **140**, 277–286 (1990).
- ¹⁵R. S. Subramanian and R. Balasubramanian, *The Motion of Bubbles and Drops in Reduced Gravity* (Cambridge University Press, 2001).
- ¹⁶J. Szymczyk and J. Siekmann, "Numerical calculation of the thermocapillary motion of a bubble under microgravity," *Chem. Eng. Commun.* **69**, 129–147 (1988).
- ¹⁷Z. Yin, L. Chang, W. Hu, Q. Li, and H. Wang, "Numerical simulations on thermocapillary migrations of nondeformable droplets with large Marangoni numbers," *Phys. Fluids* **24** (2012).
- ¹⁸C. Ma and D. Bothe, "Direct numerical simulation of thermocapillary flow based on the volume of fluid method," *Int. J. Multiphase Flow* **37**, 1045–1058 (2011).
- ¹⁹I. Seric, S. Afkhami, and L. Kondic, "Direct numerical simulation of variable surface tension flows using a volume-of-fluid method," *J. Comput. Phys.* **352**, 615–636 (2018); e-print [arXiv:1703.00327](https://arxiv.org/abs/1703.00327).
- ²⁰J. F. Zhao, L. Zhang, Z. D. Li, and W. T. Qin, "Topological structure evolution of flow and temperature fields in deformable drop Marangoni migration in microgravity," *Int. J. Heat Mass Transfer* **54**, 4655–4663 (2011).
- ²¹H. Liu, L. Wu, Y. Ba, and G. Xi, "A lattice Boltzmann method for axisymmetric thermocapillary flows," *Int. J. Heat Mass Transfer* **104**, 337–350 (2017).
- ²²L. Qiao, Z. Zeng, H. Xie, L. Zhang, L. Wang, and Y. Lu, "Modeling thermocapillary migration of interfacial droplets by a hybrid lattice Boltzmann finite difference scheme," *Appl. Therm. Eng.* **131**, 910–919 (2018).
- ²³H. Haj-Hariri, Q. Shi, and A. Borhan, "Thermocapillary motion of deformable drops at finite Reynolds and Marangoni numbers," *Phys. Fluids* **9**, 845–855 (1997).
- ²⁴B. Samareh, J. Mostaghimi, and C. Moreau, "Thermocapillary migration of a deformable droplet," *Int. J. Heat Mass Transfer* **73**, 616–626 (2014).
- ²⁵M. K. Tripathi and K. C. Sahu, "Motion of an air bubble under the action of thermocapillary and buoyancy forces," *Comput. Fluids* **177**, 58–68 (2018); e-print [arXiv:1806.06491](https://arxiv.org/abs/1806.06491).
- ²⁶M. Balla, M. K. Tripathi, K. C. Sahu, G. Karapetsas, and O. K. Matar, "Non-isothermal bubble rise dynamics in a self-wetting fluid: Three-dimensional effects," *J. Fluid Mech.* **858**, 689–713 (2019).
- ²⁷J. Chen, Z. Dagan, and C. Maldreli, "Axisymmetric thermocapillary motion of a fluid particle in a tube," *J. Fluid Mech.* **233**, 405–437 (1991).
- ²⁸H. Keh, P. Chen, and L. Chen, "Thermocapillary motion of a fluid droplet parallel to two plane walls," *Int. J. Multiphase Flow* **28**, 1149–1175 (2002).
- ²⁹L. Chang, Z. Yin, and W. Hu, "Transient behavior of the thermocapillary migration of drops under the influence of deformation," *Sci. China Phys. Mech. Astron.* **41** (2011), 960.
- ³⁰S. Mahesri, H. Haj-Hariri, and A. Borhan, "Effect of interface deformability on thermocapillary motion of a drop in a tube," *Heat Mass Transfer* **50**, 363–372 (2014).
- ³¹P. Capobianchi, M. Lappa, and M. S. Oliveira, "Walls and domain shape effects on the thermal Marangoni migration of three-dimensional droplets," *Phys. Fluids* **29** (2017).
- ³²Y. Alhendal, A. Turan, and A. Kalendar, "Wall effects on the thermocapillary migration of single gas bubbles in stagnant liquids," *Heat Mass Transfer* **53**, 1315–1326 (2017).
- ³³P. T. Brady, M. Herrmann, and J. M. Lopez, "Confined thermocapillary motion of a three-dimensional deformable drop," *Phys. Fluids* **23**, 022101 (2011).
- ³⁴Q. Kang, H. L. Cui, L. Hu, and L. Duan, "On-board experimental study of bubble thermocapillary migration in a recoverable satellite," *Microgravity Sci. Technol.* **20**, 67–71 (2008).
- ³⁵H. J. Keh and L. S. Chen, "Droplet interactions in thermocapillary migration," *Chem. Eng. Sci.* **48**, 3565–3582 (1993).
- ³⁶H. Zhou and R. H. Davis, "Axisymmetric thermocapillary migration of two deformable viscous drops analyzed the motion of two bubbles along their line of centers under the action of a uniform temperature gradient in the limit of negligible convective transport of momentum," *J. Colloid Interface Sci.* **181**, 60–72 (1996).
- ³⁷S. Nas and G. Tryggvason, "Thermocapillary interaction of two bubbles or drops," *Int. J. Multiphase Flow* **29**, 1117–1135 (2003).
- ³⁸Y. Alhendal, A. Turan, and W. I. A. Aly, "VOF simulation of marangoni flow of gas bubbles in 2D-axisymmetric column," *Procedia Comput. Sci.* **1**, 673–680 (2010).
- ³⁹Z. H. Yin, L. Chang, W. R. Hu, and P. Gao, "Thermocapillary migration and interaction of two nondeformable drops," *Appl. Math. Mech.* **32**, 811–824 (2011).
- ⁴⁰Z. Yin and Q. Li, "Thermocapillary migration and interaction of drops: Two non-merging drops in an aligned arrangement," *J. Fluid Mech.* **766**, 436–467 (2015).
- ⁴¹A. Pattamatta, A. Sielaff, and P. Stephan, "A numerical study on the hydrodynamic and heat transfer characteristics of oscillating Taylor bubble in a capillary tube," *Appl. Therm. Eng.* **89**, 628–639 (2015).
- ⁴²J. U. Brackbill, D. B. Kothe, and C. Zemach, "A continuum method for modeling surface tension," *J. Comput. Phys.* **100**, 335–354 (1992).
- ⁴³C. Kunkelmann, "Numerical modeling and investigation of boiling phenomena," Ph.D. thesis, Technische Universit at Darmstadt, 2011.
- ⁴⁴H. Liu, Y. Zhang, and A. J. Valocchi, "Modeling and simulation of thermocapillary flows using lattice Boltzmann method," *J. Comput. Phys.* **231**, 4433–4453 (2012).